Direct imaging of nanoscale magnetic interactions in minerals

Richard J. Harrison*, Rafal E. Dunin-Borkowski[†‡], and Andrew Putnis[§]

*Department of Earth Sciences, University of Cambridge, Downing Street, Cambridge CB2 3EQ, United Kingdom; [†]Department of Materials Science and Metallurgy, University of Cambridge, Pembroke Street, Cambridge CB2 3QZ, United Kingdom; and [§]Institut für Mineralogie, Corrensstrasse 24, D-48149 Münster, Germany

Edited by W. G. Ernst, Stanford University, Stanford, CA, and approved November 4, 2002 (received for review August 26, 2002)

The magnetic microstructure of a natural, finely exsolved intergrowth of submicron magnetite blocks in an ulvöspinel matrix is characterized by using off-axis electron holography in the transmission electron microscope. Single-domain and vortex states in individual blocks, as well as magnetostatic interaction fields between them, are imaged at a spatial resolution approaching the nanometer scale. The images reveal an extremely complicated magnetic structure dominated by the shapes of the blocks and magnetostatic interactions. Magnetic superstates, in which clusters of magnetite blocks act collectively to form vortex and multidomain states that have zero net magnetization, are observed directly.

Magnetite is the most strongly magnetic mineral in nature. Small particles of magnetite in single-domain (SD) or pseudo-SD magnetization states (with sizes in the range of 30–70 nm and 70 nm to 20 μm, respectively) are the dominant carriers of remanent magnetization in rocks. Larger, multidomain (MD) particles that contain magnetic domain walls would have significantly lower coercivities and thermal stabilities than SD and pseudo-SD particles (1). In most igneous rocks, the grain size of primary magnetic minerals exceeds the MD threshold. Such rocks are less likely to maintain strong and stable natural remanent magnetization (NRM) over geological times than those containing SD particles. It has long been proposed that solid-state processes such as subsolvus exsolution can generate SD magnetite particles from MD grains, thus increasing the stability of the NRM (2). Such processes are thought to be responsible for the strong and stable remanent magnetization exhibited by many rocks and have been proposed as a possible source of magnetic anomalies on Mars. However, the magnetic microstructure of finely exsolved minerals has never been observed directly at the nanometer scale.

The magnetite-ulvöspinel (Fe_3O_4-Fe_2TiO_4) system forms a complete solid solution at temperatures above ≈450°C, but has a miscibility gap at lower temperatures (3–5). Intermediate bulk compositions (termed titanomagnetites) exsolve during slow cooling, at low or buffered oxygen fugacity, to yield an intergrowth of SD or pseudo-SD magnetite-rich blocks separated by nonmagnetic ulvöspinel-rich lamellae. In this article, off-axis electron holography, a transmission electron microscopy (TEM) technique that yields a vector map of the magnetic field in a sample with nanometer resolution (6–8), is used to image the magnetic microstructure of a natural titanomagnetite intergrowth. The high spatial resolution of the technique makes it ideal for the study of nanoscale particles at the boundary between SD and pseudo-SD behavior.

Experimental Details

A finely exsolved titanomagnetite from Mount Yamaska, Quebec, one of the Monterigian Hills of Cretacious age (Cambridge University Harker Collection no. 92966) (8), was extracted from a petrographic thin section and prepared for TEM examination by using ion-beam milling. Some bulk magnetic properties of this material had been studied (2, 9), and its microstructure had been examined by using TEM (10). Electron microprobe analysis indicates a bulk composition of 42% Fe_3O_4, 39% Fe_2TiO_4, 11% $MgAl_2O_4$, and 8% $MgFe_2O_4$. TEM observations were carried out at 300 kV by using a Philips Electron Optics (Eindhoven, The Netherlands) CM300-ST equipped with a field-emission gun electron source, a Lorentz lens, an electrostatic biprism, and a Gatan (Pleasanton, CA) imaging filter.

Fig. 1*a* shows a chemical map of a representative area of the sample. Ulvöspinel-rich exsolution lamellae (red) subdivide the original titanomagnetite grain into a fairly regular array of magnetite-rich blocks (blue). The profiles in Fig. 1 *b* and *c*, which were obtained from the line marked C in Fig. 1*a*, confirm that little Ti is present in the blocks, i.e., that they are essentially pure magnetite. Similar maps reveal that Mg and Al are not present in this area in significant quantities. Chosen magnetite blocks, whose linear dimensions vary between 5 and 175 nm, are numbered in Fig. 1 so that they can be referred to below. The width of the ulvöspinel lamellae varies between 8 and 100 nm, whereas the aspect ratio of the blocks in the plane of the sample varies between 1 and 10. High-resolution images indicate that the interfaces between magnetite and ulvöspinel are either coherent or semicoherent. The thickness of the sample increases from 70 nm at the top to 195 nm at the bottom of region B in Fig. 1, which will be examined in detail below. The blocks in this region are therefore roughly equidimensional.

The microscope geometry for off-axis electron holography is shown schematically in Fig. 2*a*. The sample is examined by using coherent illumination from a field-emission gun, with the region of interest positioned so that it covers approximately half the field of view. A positive voltage applied to an electrostatic biprism causes an electron wave that has passed through the sample to overlap with a reference wave that has passed through vacuum. Holographic fringes form in the overlap region due to interference between the sample and reference waves. Fig. 2*b* shows a hologram obtained from the region marked A in Fig. 1*a*. The amplitude and phase of the electron wave leaving the sample are recorded in the intensity and the position of the holographic fringes, respectively (11). The phase shift is sensitive both to the thickness and composition of the sample and to the in-plane component of the magnetic induction integrated in the incident beam direction. Once the magnetic contribution to the phase has been extracted, a picture of the magnetic field lines in the sample is obtained simply by adding contours to the phase image. Since both thickness and composition vary in magnetite-ulvöspinel intergrowths, these effects must be subtracted from the raw phase image to yield the magnetic contribution to the phase. Fortunately, as the mean inner potentials of magnetite and ulvöspinel are exactly equal, only a thickness correction is required. The thickness was determined from t/λ_i maps obtained by using electron energy-loss spectroscopy (where λ_i is the

This paper was submitted directly (Track II) to the PNAS office.

Abbreviations: SD, single domain; MD, multidomain; NRM, natural remanent magnetization; TEM, transmission electron microscopy.

[‡]To whom correspondence should be addressed. E-mail: rafal.db@msm.cam.ac.uk.

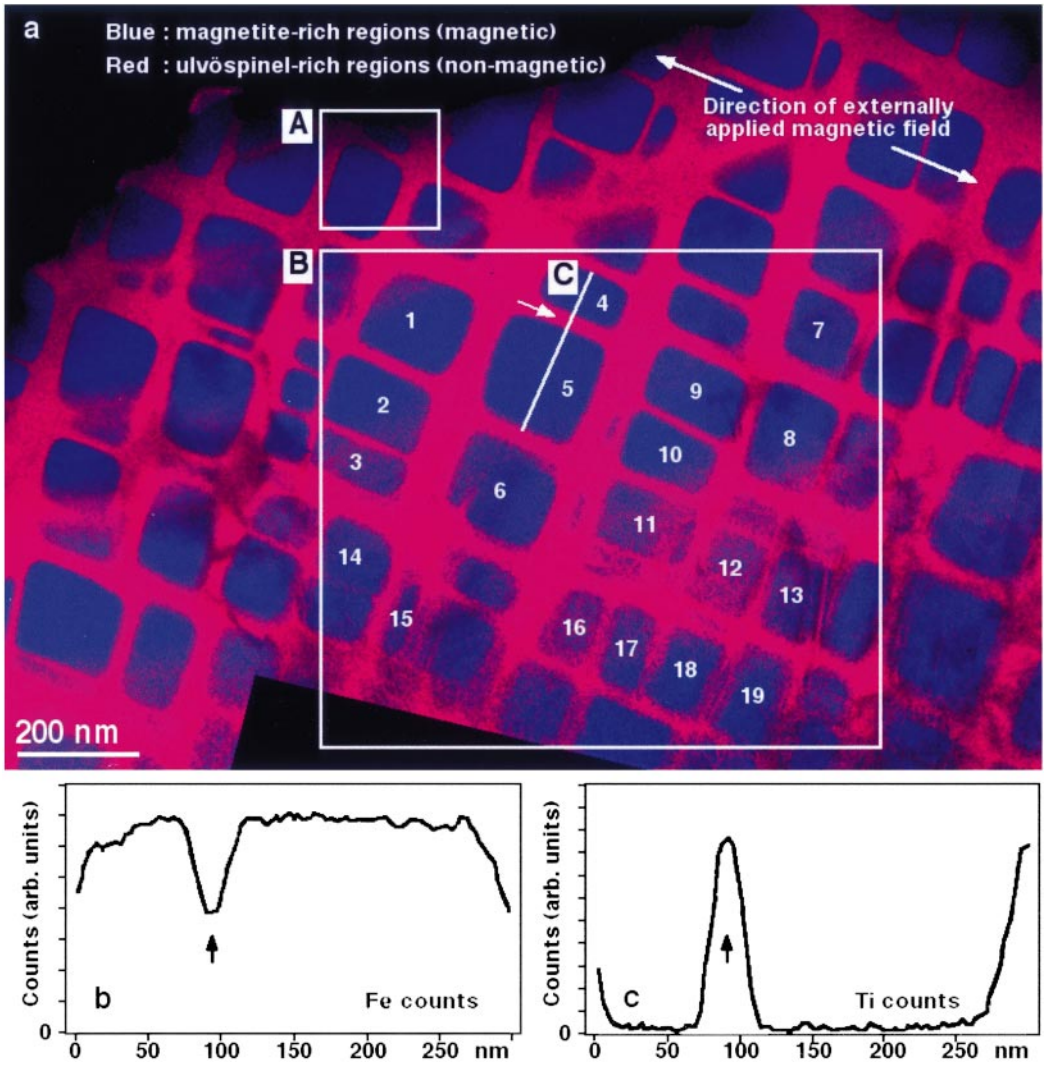

Fig. 1. (*a*) Chemical map of titanomagnetite sample examined in this study, acquired by using three-window, background-subtracted elemental mapping at the Fe $L_{2,3}$ and Ti $L_{2,3}$ edges in a Gatan imaging filter (GIF). The GIF separates electrons that have lost energy in the sample due to inelastic scattering from elastically scattered electrons and refocuses them to form an image of the sample. After suitable background correction, the image corresponds to a chemical map, whose intensity is proportional to the concentration of the appropriate element projected through the thickness of the sample. Blue and red correspond to Fe and Ti concentrations, respectively. The blue regions are magnetic and are rich in magnetite (Fe_3O_4), whereas the red regions are nonmagnetic and rich in ulvöspinel (Fe_2TiO_4). The numbers refer to individual magnetite-rich blocks, which are discussed in the text. The boxes marked A and B correspond to regions referred to in subsequent figures. (*b* and *c*) Line profiles obtained from the Fe and Ti chemical maps, respectively, along the line marked C in *a*. The short arrows mark the same point in the three pictures.

inelastic mean-free-path of electrons in the sample and is estimated to be ≈170 nm for the present sample at 300 kV). The constant of proportionality between t/λ_i and the mean inner potential contribution to the phase was determined by least-squares fitting to data collected near the edge of the wedge-shaped sample (where the magnetic contribution is negligible), on the assumption that the mean inner potential of magnetite is 17 V. (The ratio of the magnetic contribution to the phase shift across a magnetite block to the mean inner potential contribution was typically between 0.15 and 0.30.)

In a conventional electron microscope, the objective lens creates a large vertical magnetic field at the position of the sample. For holography of magnetic materials, the objective lens is switched off and a Lorentz lens is used to examine the sample in field-free conditions. By partially exciting the objective lens and tilting the sample, different in-plane components of magnetic field can be applied to the sample *in situ*, allowing reversal mechanisms, hysteresis loops, and remanent states to be studied. In the present work, remanent states were studied by initially tilting the sample to the maximum available angle of 41° in zero field and turning the objective lens on fully to saturate the sample in one direction. This process provided a known starting point from which further fields could be applied. The objective lens was then turned off, the sample was tilted to 41° in zero field in the opposite direction, and the objective lens was partially excited to apply a known in-plane component of magnetic field to the sample in the opposite direction. The objective lens was switched off and the sample was tilted back to 0° in zero field to record the hologram. This procedure was repeated for a number of different applied fields.

Results

Fig. 3 shows the magnetic microstructure of region B marked in Fig. 1*a* for eight different remanent states. The results were obtained after applying the in-plane fields indicated in Fig. 3. (For in-plane applied fields of 1,340, 628, and 225 Oe, with the

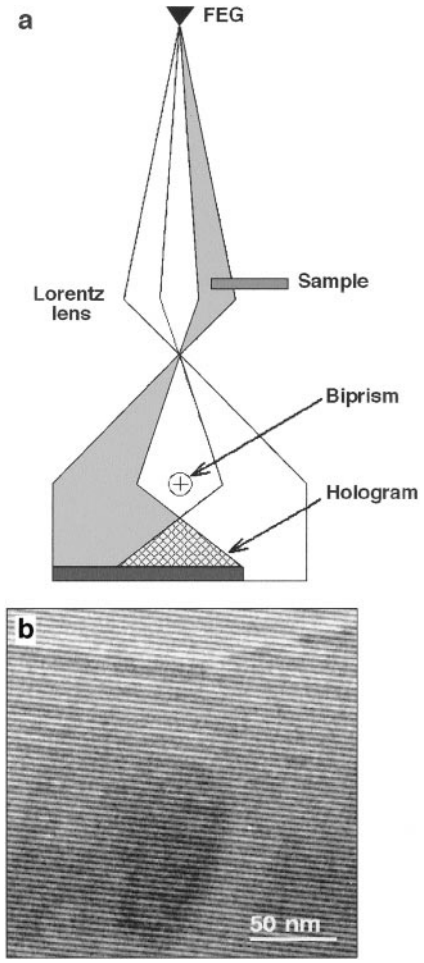

Fig. 2. (*a*) Schematic illustration of set-up used for generating off-axis electron holograms. The sample occupies approximately half the field of view. Essential components are the field emission electron gun (FEG) electron source, which provides coherent illumination, and the positively charged electrostatic biprism (a thin gold-coated quartz fiber, ≈0.6 μm in diameter), which causes overlap of the object and (vacuum) reference waves. The resulting holographic interference pattern is recorded digitally. The Lorentz lens allows imaging of magnetic materials in close-to-field-free conditions. (*b*) Off-axis electron hologram obtained from region A in Fig. 1*a*. The edge of the sample is close to the top of the picture, while the dark area results from diffraction contrast from one of the magnetite-rich regions. The biprism voltage is 200 V, and the holographic interference fringe spacing is 3.5 nm.

sample tilted by 41°, the out-of-plane component of the applied field is 1,520, 713, and 255 Oe, respectively.) The direction and the spacing of the black contour lines provide the direction and the magnitude of the magnetic induction in the plane of the sample, which can be correlated with the positions of the magnetite blocks (outlined in white). The direction of the local induction is also indicated by colors, according to the color wheel shown at the bottom of Fig. 3, and arrows. The spacings of the contours in the blocks decrease slightly from the top to the bottom, reflecting the increase in the thickness of the sample. The recorded phase images have been smoothed very slightly to remove noise, so that the spatial resolution of the magnetic information is estimated to be between 10 and 20 nm.

General Observations. Fig. 3 shows that the magnetic domain structure in this sample is extremely complex. Although the magnetization is never saturated in the direction of the applied field, analysis shows that the average magnetization direction is parallel (or antiparallel) to this direction. The contours outside the blocks are associated with stray interaction fields and are, on average, more widely spaced than the internal contours.

The ability to differentiate between internal and external contributions to the magnetic field allows two fundamental issues related to the magnetic behavior of fine-scale intergrowths to be addressed: the magnetization states of individual blocks and the collective behavior of the grain as a whole. The first point has been the subject of intense study with micromagnetic simulations (12), which predict the existence of "flower" and "vortex" states in isolated magnetite cubes of equivalent size to those described here. If the blocks can adopt vortex rather than SD states, then the magnetic properties of the mineral (e.g., its remanent magnetization and coercive force) are changed fundamentally. It is known from macroscopic measurements that magnetostatic interactions between blocks play a crucial role in determining the remanent properties of rocks. Interactions result in a pronounced shearing of the hysteresis loop and a reduction in remanent magnetization. They also provide a potential mechanism for the acquisition of self-reversed thermoremanent magnetization, i.e., the acquisition of a remanent magnetization antiparallel to the direction of the applied field.

The details of the magnetic microstructure do not reverse exactly when the same in-plane component of magnetic field is applied in opposite directions. Some blocks (e.g., block 5) point in almost the same direction irrespective of the magnitude and direction of the applied field. This asymmetry may result from the presence of an out-of-plane component of the applied magnetic field, which has been observed to affect vortex helicity in lithographically patterned magnetic elements (13). Alternative explanations include the region of interest not being precisely flat at zero tilt and the effect of the shape of the ion-beam thinned TEM sample. Although these effects should be taken into consideration, they do not affect most of the conclusions presented below.

Magnetization States of Individual Blocks. The magnetite blocks are primarily in nonuniform SD states (e.g., block 5 in all of Fig. 3) or single vortex states (e.g., block 6 in Fig. 3 *a* and *h*). Some blocks are reminiscent of a flower state, with the contour lines fringing out at their surface (e.g., block 9 in Fig. 3*e*). Others have a large component of their magnetization perpendicular to the plane of the sample, and therefore show few contours (e.g., blocks 7 and 12 in Fig. 3*g*).

The smallest block observed to form a vortex (number 14) has dimensions of 115 × 90 × 145 nm. These dimensions are larger than the predicted minimum size of 70 nm for vortices to form in isolated cubes of magnetite[11]. Nonuniform SD states are observed in blocks as large as 165 × 160 × 100 nm, which is smaller than the maximum size of 200 nm predicted for the breakdown of SD to vortex states in isolated magnetite cubes. No blocks significantly larger than 200 nm were present in the areas studied, so the presence of larger SD blocks cannot be ruled out.

The SD and vortex states represent alternative local energy minima for blocks of this size, which can adopt either state depending on the direction and the magnitude of the applied magnetic field, as well as on the magnetization states of their neighbors. (Compare, for example, the magnetization state of block 6 in Fig. 3 *a* and *b*.) The abundance of SD states implies that they have a lower energy than vortex states in the presence of strong interactions. For isolated cubes of magnetite, micromagnetic simulations predict the opposite, with the vortex state having a lower energy than the SD state over the size range 70 to 200 nm. The demagnetizing energy, which normally destabilizes the SD state with respect to the vortex state in isolated particles, is greatly reduced in an array of strongly interacting particles. Hence, care must be taken when using simulations of

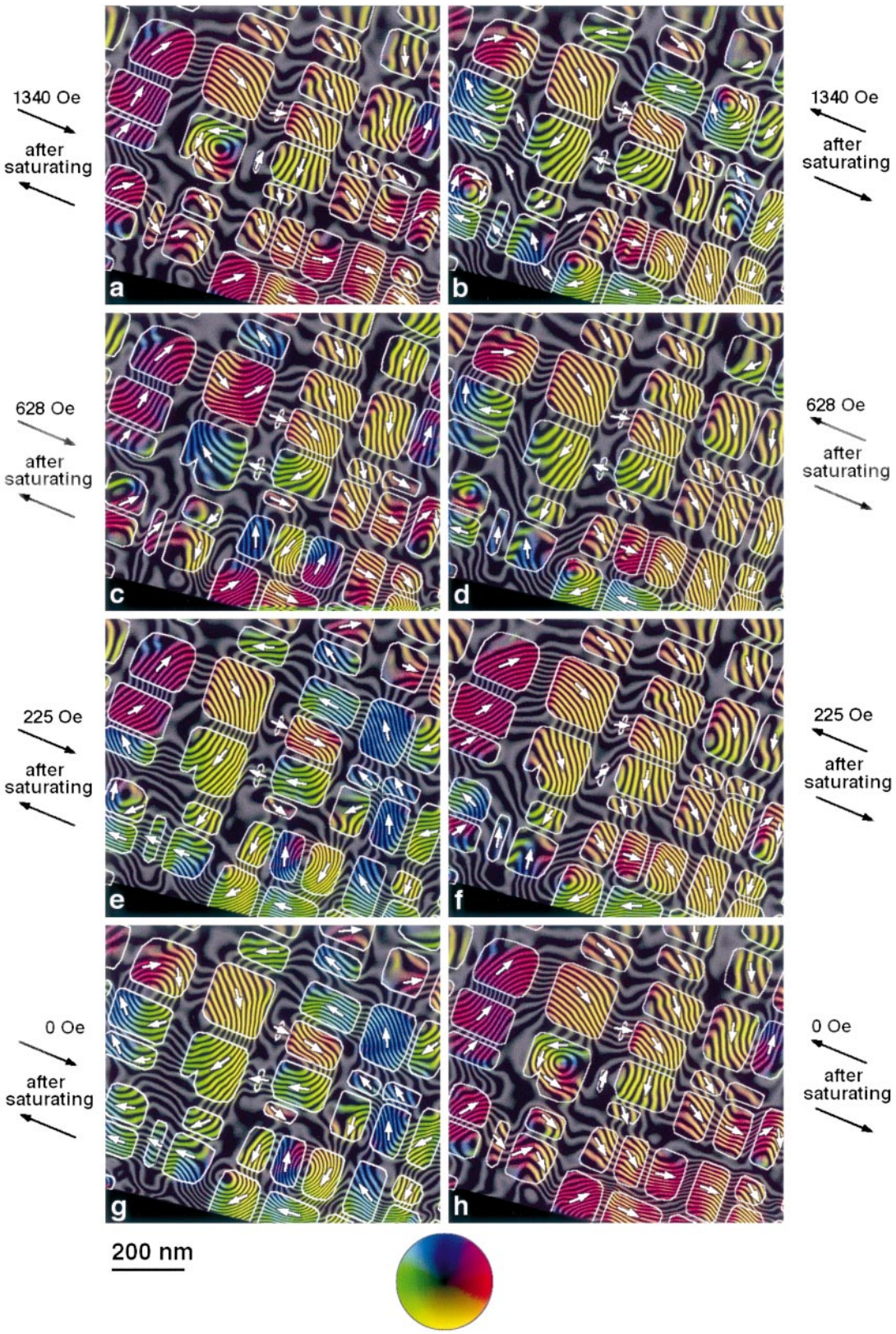

Fig. 3. Magnetic microstructure of region B in Fig. 1*a* measured by using electron holography. Each image corresponds to a different magnetic remanent state, acquired with the sample in field-free conditions. The outlines of the magnetite-rich regions are marked in white, while the direction of the measured magnetic induction is indicated both using arrows and according to the color wheel shown at the bottom (red = right, yellow = down, green = left, blue = up). The spacing of the black contours is inversely proportional to the in-plane component of the magnetic induction projected in the incident electron beam direction, and thus provides a measure of the strength of the magnetic field in the plane of the sample. Images *a*, *c*, *e*, and *g* were obtained after applying a large (>10,000 Oe) field toward the top left of each picture, then the indicated field toward the bottom right, after which the external magnetic field was removed for hologram acquisition. Images *b*, *d*, *f*, and *h* were obtained after applying identical fields in the opposite directions.

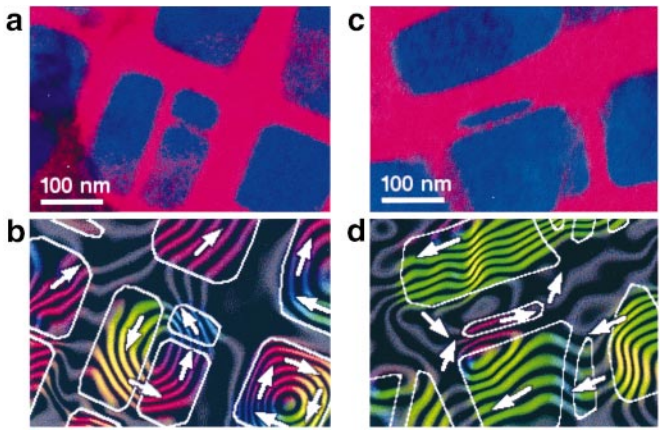

Fig. 4. (*a* and *c*) Chemical maps (blue = Fe, red = Ti) from two regions not shown in Figs. 1 and 3. (*b* and *d*) The corresponding magnetic microstructures, in the same format as Fig. 3. (*b*) Three adjacent magnetite-rich regions combining to form a single vortex; (*d*) a small region that is magnetically antiparallel to its larger neighbors.

isolated particles to predict the domain states of interacting particles in a fine-scale intergrowth.

Differences between the magnetic moments of individual SD blocks can be seen in Fig. 3. For example, block 8 in Fig. 3*e* is magnetized roughly north-northwest (blue), whereas in Fig. 3*f* it is magnetized roughly south-southeast (yellow). It contains an off-centered vortex in Fig. 3*b*, suggesting that magnetization reversal in this block could occur via the formation, displacement, and subsequent annihalation of a vortex state (14), rather than by coherent rotation of the SD moment.

The preferred magnetization direction of a SD particle is determined by a number of factors, including magnetocrystalline anisotropy, shape anisotropy, and magnetostatic interactions with neighboring particles. The influence of magnetocrystalline anisotropy, which results in preferred magnetization directions parallel to <111> in magnetite, is relatively small. In the present study, it is apparent from Fig. 3 that the magnetization directions of the blocks are determined primarily by shape anisotropy and interactions. Shape anisotropy dominates when the magnetization lies parallel to the long axis of a block (e.g., in blocks 9–11 and 16–18 in Fig. 3 *e* and *g*). In other cases, magnetostatic interactions force the magnetization to point perpendicular to the long axis (e.g., blocks 15 and 19 in Fig. 3*h*). The magnetization can also lie parallel to the body diagonal (e.g., blocks 5 and 8 in Fig. 3 *e* and *g*).

Collective Behavior. In Fig. 3, several blocks are observed to act collectively to form magnetic "superstates" that would normally be observed in single, much larger magnetized regions. A common example is where two or more blocks interact to form a vortex superstate. Two-, three-, and five-block vortex superstates are visible in Fig. 3 (e.g., blocks 1 and 2 in Fig. 3*g* and blocks 1–3, 5, and 6 in Fig. 3*e*). A similar superstate involving three elongated blocks is shown in Fig. 4*b* and schematically in Fig. 5*a*. The absence of closely spaced contours between the superstate and the adjacent single vortex in Fig. 4*b* shows the efficiency with which stray interaction fields are eliminated in the intervening ulvöspinel. Flux closure is achieved with considerably less curvature of magnetization within the three-component blocks than in the adjacent conventional vortex, reducing the exchange energy penalty associated with the nonuniform magnetization.

A second example of collective behavior involves the interaction of a chain of blocks to form a SD superstate magnetized parallel to the chain axis but perpendicular to the easy axes of the

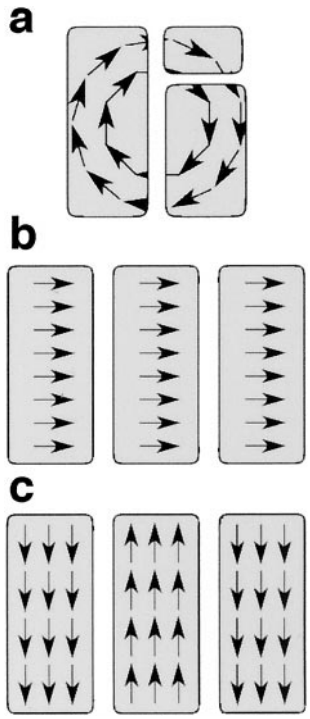

Fig. 5. Schematic diagrams showing some of the possible magnetization states of three closely spaced regions of magnetic material.

individual blocks. This behavior is illustrated schematically in Fig. 5*b* and can be found in several places in Fig. 3 (e.g., blocks 16–18 in Fig. 3 *a*, *b*, *d*, *f*, and *h*). If the three blocks are instead magnetized perpendicular to the chain axis, then a third superstate equivalent to a three-domain particle is generated (Fig. 5*c*). The central block is now magnetized antiparallel to the blocks on either side of it. Several examples of this behavior can be found (e.g., blocks 16–18 and blocks 9–11 in Fig. 3 *c*, *e*, and *g*).

A similar phenomenon occurs when a small block is sandwiched between larger ones, as shown in Fig. 4 *c* and *d*. In Fig. 4*d*, the two largest blocks are colored green, indicating that they are both magnetized in the same direction. The small block in between them is colored red, indicating that it is magnetized in the opposite direction. The magnetization in the small block follows the flux return paths of its larger neighbors, and the resulting dipole-like magnetic field is clearly resolved. Fig. 4 provides a direct observation of one of the fundamental causes of self-reversed thermoremanent magnetization. The blocking temperature of a particle, below which the magnetization direction of a particle becomes "locked in" during cooling in the presence of an applied magnetic field, is determined by its size. The present geomagnetic field (0.3–0.6 Oe) is much lower than the switching fields of the magnetite particles examined here. Larger blocks have a higher blocking temperature than smaller blocks and will be first to acquire a thermoremanent magnetization parallel to the applied field on cooling. The magnetization directions of smaller blocks become locked in at a lower temperature and may point antiparallel to the applied field direction due to strong magnetostatic interactions with their neighbors, as in the partially self-reversed configuration shown in Fig. 4*d*. Similar interactions are likely to constrain the magnetization directions of blocks that are small enough to be superparamagnetic at room temperature if they were isolated, as observed with electron holography for 20-nm magnetite crystals arranged in chains in magnetotactic bacteria (15). Full self-reversal could be achieved if the volumetric proportion of smaller blocks was

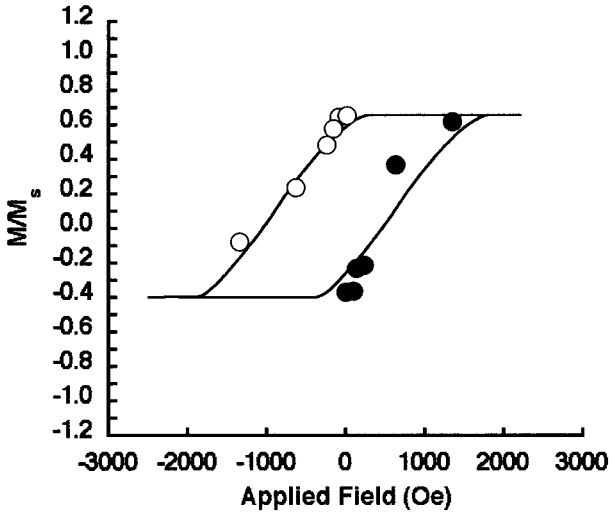

Fig. 6. Remanent hysteresis loop obtained from the images shown in Fig. 3 by plotting the average fraction of the measured magnetic induction in the magnetite-rich blocks in the direction of the applied field. The graph tends to a value below unity because the magnetic microstructure is never saturated in the applied field direction in the remanent state.

greater than that of larger blocks and the demagnetizing field of the larger blocks was sufficient to overcome the applied field.

Macroscopic Behavior. As well as providing detailed images of magnetic domain states at the nanometer scale, the measurements yield semiquantitative information about the net magnetic behavior of the sample at mesoscopic-length scales. Fig. 6 shows a "remanent hysteresis loop" determined from images such as those shown in Fig. 3. The circles indicate the fraction of the magnetization in the blocks that points in the direction of the applied field. The open and closed circles correspond to opposite directions of the applied field. The fitted curve tends to a value well below unity because the magnetization is never saturated in the remanent state. This graph provides an upper limit for the ratio of saturation remanent magnetization to saturation magnetization (M_{rs}/M_s) of $\approx$0.5. A lower limit for M_{rs}/M_s of $\approx$0.2 is obtained from the slope of the recorded magnetic contribution to the holographic phase shift. Values of M_{rs}/M_s of $\approx$0.2–0.5 are characteristic of SD behavior.

An alternative test of SD vs. MD behavior is provided by the ratio of the coercivity of remanence to the coercivity (H_{cr}/H_c). Fig. 6 yields an estimate for H_{cr} of 700 $\pm$ 200 Oe for this region of the sample. Typical estimates (12) for the maximum coercivities H_c of isolated magnetite blocks of this size are $\approx$100 Oe, yielding a lower bound of $H_{cr}/H_c \approx 7$. This is above the limit of $H_{cr}/H_c \geq 4$ normally associated with MD behavior (16). (Isolated SD grains would have $1 < H_{cr}/H_c < 2$.) Similar MD-like behavior has been observed by using conventional hysteresis measurements of synthetic intergrowths of magnetite and spinel ($MgAl_2O_4$) (17).

Discussion

The unusual combination of MD- and SD-like macroscopic properties means that the ability of fine-scale intergrowths to carry strong and stable NRM is not clear-cut. Strong magnetostatic interactions between neighboring blocks create a large demagnetizing field in the grain as a whole. These interactions cause a reduction in magnetization due to the spontaneous formation of vortex or MD superstates when the applied field is removed. Coarsening would reduce the number of magnetite blocks per unit volume, resulting in weaker interactions and more SD-like behavior. Coarsening would, however, increase the average block size and the likelihood of vortex states. The low magnetocrystalline anisotropy of magnetite and the roughly equidimensional morphology of the blocks results in low intrinsic coercivities. As a result, a block is able to respond readily to the demagnetizing field created by its neighbors. Microstructures with a more lamellar microstructure would have increased shape anisotropy and a greater potential for maintaining stable NRM. Nevertheless, it is clear from Fig. 6 that many blocks are sufficiently below their blocking temperature to prevent reorientation of their magnetic moments in response to interactions with their neighbors, leading to SD-like values of M_{rs}/M_s. Understanding the behavior at higher temperatures, in smaller fields, and over longer time scales is now of primary importance.

The recent discovery of large crustal magnetic anomalies in the southern hemisphere of Mars (18, 19) has reignited the debate over which minerals are capable of maintaining strong remanent magnetizations over the $\approx$4 billion years since there was last a magnetic field on Mars. Proper identification of the minerals and/or microstructures responsible for the anomalies is a prerequisite for developing a realistic geophysical model for the creation of the Martian crust. The generation of SD magnetite by exsolution and/or oxidation processes in titanomagnetite has been suggested as a possible source of stable remanent magnetization on Mars (20). In both cases, the microstructures would be similar to those observed here. It is assumed that the cooling rate would be slow enough to allow phase separation but fast enough to ensure that the resulting magnetite blocks are of SD, rather than MD, size. The required cooling rate is determined by analogy with terrestrial rocks and is used to constrain the geophysical model. Slower cooling rates in terrestrial rocks result in more coarsely exsolved titanomagnetites with a more lamellar morphology and a greater ability to store stable NRM (10). Such considerations have implications for the cooling-rate constraints used in geophysical models of the Martian crust.

We are grateful to the Royal Society, the Engineering and Physical Sciences Research Council, and the Deutsche Forschungsgemeinschaft for support.

1. Dunlop, D. J. & Özdemir, Ö. (1997) *Rock Magnetism, Fundamentals, and Frontiers* (Cambridge Univ. Press, Cambridge, U.K.).
2. Davis, P. M. & Evans, M. E. (1976) *J. Geophys. Res.* **81,** 989–994.
3. Vincent, E. A., Wright, J. B., Chevallier, R. & Mathieu, S. (1957) *Miner. Mag.* **31,** 624–655.
4. Price, G. D. (1981) *Am. Mineral.* **66,** 751–758.
5. Lindsley, D. H. (1981) *Am. Mineral.* **66,** 759–762.
6. Tonomura, A. (1992) *Adv. Phys.* **41,** 59–103.
7. Midgley, P. A. (2001) *Micron* **32,** 167–184.
8. Feininger, T. & Goodacre, A. K. (1995) *Can. J. Earth Sci.* **32,** 1350–1364.
9. Evans, M. E. & Wayman, M. L. (1974) *Geophys. J. R. Astron. Soc.* **36,** 1–10.
10. Price, G. D. (1980) *Phys. Earth Planet. Inter.* **23,** 2–12.
11. Dunin-Borkowski, R. E., McCartney, M. R., Kardynal, B., Parkin, S. S. P., Scheinfein, M. R. & Smith, D. J. (2000) *J. Microsc.* **200,** 187–204.
12. Williams, W. & Wright, T. M. (1998) *J. Geophys. Res.* **103,** 30537–30550.
13. Dunin-Borkowski, R. E., McCartney, M. R., Kardynal, B., Smith, D. J. & Scheinfein, M. R. (1999) *Appl. Phys. Lett.* **75,** 2641–2643.
14. Dunin-Borkowski, R. E., McCartney, M. R., Kardynal, B. & Smith, D. J. (1998) *J. Appl. Phys.* **84,** 374–378.
15. Dunin-Borkowski, R. E., McCartney, M. R., Frankel, R. B., Bazylinski, D. A., Pósfai, M. & Buseck, P. R. (1998) *Science* **282,** 1868–1870.
16. Day, R., Fuller, M. D. & Schmidt, V. A. (1977) *Phys. Earth Planet. Inter.* **13,** 260–267.
17. Harrison, R. J. & Putnis, A. (1996) *Am. Mineral.* **82,** 131–142.
18. Acuña, M. H., Connerney, J. E. P., Ness, N. F., Lin, R. P., Mitchell, D., Carlson, C. W., McFadden, J., Anderson, K. A., Reme, H., Mazelle, C., *et al.* (1999) *Science* **284,** 790–793.
19. Connerney, J. E. P., Acuña, M. H., Wasilewski, P. J., Ness, N. F., Reme, H., Mazelle, C., Vignes, D., Lin, R. P., Mitchell, D. L. & Cloutier, P. A. (1999) *Science* **284,** 794–798.
20. Nimmo, F. (2000) *Geology* **28,** 391–394.